Oilfield-produced water treatment with SiC-coated alumina membranes

Qin, Guangze; Liu, Yiman; Rietveld, Luuk C.; Heijman, Sebastiaan G.J.

Important note
To cite this publication, please use the final published version (if applicable).
Please check the document version above.

Oilfield-produced water treatment with SiC-coated alumina membranes☆

Guangze Qin [a,*], Yiman Liu [b], Luuk C. Rietveld [a], Sebastiaan G.J. Heijman [a]

[a] Section of Sanitary Engineering, Department of Water Management, Faculty of Civil Engineering and Geosciences, Delft University of Technology, Stevinweg 1 2628 CN Delft, the Netherlands
[b] IHE-Delft Institute for Water Education, Water Supply, Sanitation and Environmental Engineering Department, Westvest 7 2611 AX Delft, the Netherlands

ARTICLE INFO

ABSTRACT

During the extraction of fossil fuels, a complex waste stream is produced simultaneously, also known as produced water (PW). Membrane filtration is a promising technology that can successfully enable the treatment and reuse of PW. Silicon carbide (SiC) membranes are preferred for PW treatment, due to their low (ir)reversible fouling compared to other ceramic membranes. However, full SiC membrane is expensive and thus economically less feasible. Therefore, we established a method for coating SiC on alumina (Al₂O₃) ultrafiltration membranes, based on low-pressure chemical vapor deposition at 860 °C. In the presented study the fouling resistance and behavior of these novel membranes, with various pore sizes and under different operating conditions, including flux and crossflow velocity, were evaluated. We also used Al₂O₃ membranes and SiC-coated Al₂O₃ membranes in constant flux mode to treat real oilfield PW with high salinity (142 mS/cm) and COD (22670 mg/L). Additionally, the fouling mechanisms in the SiC-coated and Al₂O₃ membranes were analyzed with the help of Focused Ion Beam-Scanning Electron Microscopy imaging. The major findings were that pore blockage served as the initial (irreversible) fouling mechanism and that the (reversible) cake layer, a mixture of organic and inorganic components, dominated the rest of the filtration cycle, where the SiC coated membrane performed better than the original alumina membrane. In addition, it was found that the application of the SiC coating, and the selection of the appropriate pore size (62 nm) and crossflow velocity (0.8 m/s) increased the fouling mitigation, potentially advancing the utilization of ultrafiltration in treating saline PW for reuse purposes.

1. Introduction

The substantial amount of produced water (PW), generated from the oil and gas industry, represents a source of oily wastewater that poses a threat to marine ecosystems [1–3]. Several authors have studied various treatment technologies to enhance PW reuse [4–9]. Microfiltration (MF) [4], electro flocculation [5], ultrafiltration (UF) [6], membrane distillation [7,8], electrodialysis (ED)[9], adsorption [10], and advanced oxidation [10] are some of the methods that have been documented. Regarding oil, grease, and colloidal particle removal, membrane separation technologies appear promising for pretreating PW for desalination. However, fouling is the primary challenge for PW treatment using membranes, caused by the accumulation of particles and/or oil droplets on the membrane surface or within its pores. Water quality, operational conditions, and membrane properties influence the extent of fouling, resulting in permeability reduction during PW treatment. The main water characteristics determining the severity of fouling on the membrane surface are the content of organic matter, measured as total organic carbon (TOC), suspended solids, measured as total suspended solids (TSS), salts, measured as total dissolved solids (TDS), and oil and grease concentrations. In addition, the particle size of the suspended solids in water can play a determining role during membrane fouling [4,5]. Additionally, hydrodynamic and operational conditions, such as cross-flow velocity (CFV), operational flux, and backwash conditions, affect membrane fouling [11]. Finally, the fouling severity is related to the pore geometry, hydrophilicity, and surface charge of the membrane [12].

Polymeric membranes, including polyvinylidene fluoride (PVDF), polysulfide (PS), and polyether sulfone (PES), are commonly used for PW filtration [4,6,13]. He et al. reported that PVDF (polyvinylidene difluoride) MF membranes have successfully been applied for treating shale flowback water, which consisted of the injected fracturing fluid and the connate water of the formation [4]. However, ceramic membranes have gained popularity in treating PW due to a higher

---

☆ This article is part of a special issue entitled: 'ISPT 2024' published in Separation and Purification Technology.
* Corresponding author.
   E-mail address: G.Qin@tudelft.nl (G. Qin).

mechanical and chemical stability, compared with polymeric membranes [14–17]. These ceramic membranes have been produced from various materials, including zirconium oxide (ZrO_2), alumina (Al_2O_3), and titanium oxide (TiO_2)[12,18]. Zsirai et al. have reported that, although SiC MF membranes showed the highest water flux during filtration of the PW at constant pressure mode, they also showed the largest fouling, compared with SiC UF and TiO_2 UF/MF membranes. This was attributed to its highest initial flux, which was observed to be ten times greater than that of other ceramic membranes at the same pressure [14]. In practice, water treatment plants operate in a constant flux crossflow mode to avoid buffering after or before the other treatment steps, and to date, fouling of SiC MF/UF membranes treating real PW in constant flux crossflow mode has, to the authors' knowledge, not yet been studied.

During the treatment of PW with high salinity, the hydrophilicity of the membrane plays a crucial role in membrane fouling, since it has been reported that the zeta potential of oil droplets in PW is close to 0 mV when the NaCl concentrations of PW are higher than 50,000 mg/L [19]. Therefore, some studies have focused on the improvement of the hydrophilicity of membranes by modification techniques, such as low-pressure chemical vapor deposition (LPCVD) [20] and atomic layer deposition (ALD) [21] on the pristine membranes, to alleviate membrane fouling and achieve a better filtration efficacy. These studies have, however, mainly focused on the effect of hydrophilicity on reversible fouling because of practical reasons. Field Emission Scanning Electron Microscopy (FE-SEM) typically provides surface images and, thus, cannot directly access the internal structure of the ceramic membrane and cannot provide insight into the third dimension (depth) of the fouling layer [22]. However, Focused Ion Beam-Scanning Electron Microscopy (FIB-SEM) is a powerful tool for visualizing irreversible fouling by producing artifact-free cross sections with high-resolution (5–10 nm) ultrastructural details [23], allowing for quantitative comparison across the different membranes [24], but, to the authors' knowledge, has not yet been applied to ceramic membranes.

Pretreatment processes to alleviate the fouling, such as sedimentation, coagulation, and rapid sand filtration, are mostly performed before the UF process [25]. In the present study, for the first time, direct ceramic UF of real PW was conducted, using the SiC-coated UF membranes in constant flux mode. We established a method for producing SiC-Al_2O_3 UF membranes based on LPCVD. Firstly, the effect of the salinity on membrane fouling was determined by filtering the synthetic O/W emulsions. Secondly, the fouling resistance and behavior were evaluated under various pore sizes and operating conditions (flux, CFV) using two types of real PW with varying water quality. Finally, the (ir) reversible fouling transition mechanisms were investigated using FIB-SEM images.

2. Materials and methods

2.1. Materials and synthetic O/W emulsions preparation

Sodium hydroxide (1.09141, Sigma-Aldrich, the Netherlands) and citric acid (251275, Sigma-Aldrich, the Netherlands) were chosen for the chemical cleaning of the fouled membranes. Detailed information about the chemicals and procedure of the synthetic O/W emulsion preparation is included in the supporting information S1.

2.2. Membrane preparation

Commercial single-channeled tubular Al_2O_3 membranes were purchased from CoorsTek, the Netherlands of which the selective and support layers are made of α-alumina. The pore sizes of the two selective layers and the support layer, as provided by the manufacturer, are 100, 200, and 600 nm, respectively. The alumina membranes with these pore sizes exhibited measured permeabilities of 350 ± 10, 478 ± 21, and 985 ± 64 Lm^{-2}h^{-1}bar^{-1}, respectively.

SiC-coated membranes were prepared by LPCVD. A schematic of the LPCVD system is shown in Fig.S1; Dichlorosilane (SiH_2Cl_2) and acetylene (C_2H_2) were chosen as precursors for the SiC layers deposition. The deposition temperature was 860 °C, the precursors flow ratio (SiH_2Cl_2/C_2H_2) was 6.7 and the deposition time was 20 min [26], as recommended for the formation of polycrystalline SiC [27,28]. The pristine 100, 200, and 600 nm Al_2O_3 membranes and the corresponding SiC-coated membranes are referred to as A0, A0-200, A0-600, A20, A20-200, and A20-600, respectively.

2.3. Membrane characterization

The water contact angle (WCA) of the A0 membranes and A20 membranes was determined by Dataphysics OCA25, Germany. The zeta potential of flat sheet A0 and A20 membranes, with salinities from 10^{-3}M to 10^{-2}M, was measured by SurPASS 3 (Anton Paar, Graz, Austria), which was coated in the same way as the tubular membrane. In addition, as it is difficult to measure the zeta potential of the membrane at high salinity (10^{-1}M) by SurPASS 3, the zeta potential of the membranes at 10^{-1}M salinity was estimated using the Freundlich ion adsorption model [29], as shown in Fig.S2. SEM measurements of virgin and fouled membranes were conducted using FEI Nova NanoSEM 450 and Energy Dispersive X-ray (EDX) spectroscopy. FIB-SEM images were acquired using a 10 kV accelerating voltage and an 800 pA ion beam. The actual mean pore size was obtained by capillary flow porometry (Porolux^{TM} Revo, IBFT GmbH, Germany).

2.4. Produced water characterization

Two types of PW, provided by the Norwegian Technology company, were characterized. The first PW sample (PW A) was collected from the Mongstad refinery, originating from the Troll field. The second PW (PW B) was a mix of batches obtained from the SAR Dusavik offshore base collected from various oilfields in southern Norway. The PW samples were kept at a temperature of 4 °C until they were further processed. Typically, the PW from oil fields tends to exhibit high levels of TOC and salinity compared to the PW from gas production facilities [30]. We primarily analyzed membrane fouling caused by high-salinity PW B, with relatively low-salinity PW A as the control group for comparison.

The pH and electrical conductivity of the PW were respectively measured by multiparameter benchtop meters (inoLab® Multi 9630 IDS – WTW). The droplet sizes and distributions were measured using a Bluewave particle size analyzer (Microtrac, USA). TSS and TDS in the feed and permeate water were measured following the Standard Methods [31]. The measurement and rejection of oil and COD concentration of both feed and permeate are described in the supporting information (Fig. S3 and Fig.S4).

2.5. Estimation of threshold flux

The threshold flux was estimated using the flux stepping method [32,33]. The average TMP (TMP$_{avg}$) was then calculated and used to determine the threshold flux. Fluxes ranging from 20 Lm^{-2}h^{-1} to 55 Lm^{-2}h^{-1}, with intervals of 5 Lm^{-2}h^{-1}, were employed in the flux stepping tests, and each step lasted 20 min.

2.6. Fouling experiments with synthetic and real produced water

2.6.1. Constant permeate flux crossflow fouling experiments

A constant permeate flux crossflow setup (Fig. 1) was employed for synthetic O/W emulsions and real PW filtration experiments. The concentrate stream was recirculated to the feed during filtration, having a negligible effect on the feed concentration, while the feed pump provided a stable permeate flux (DDA12-10, Grundfos, Denmark). The constant CFVs were controlled by a circulation gear pump (VerderGear Process H1F, Verder Liquids, the Netherlands). The fouling experiments
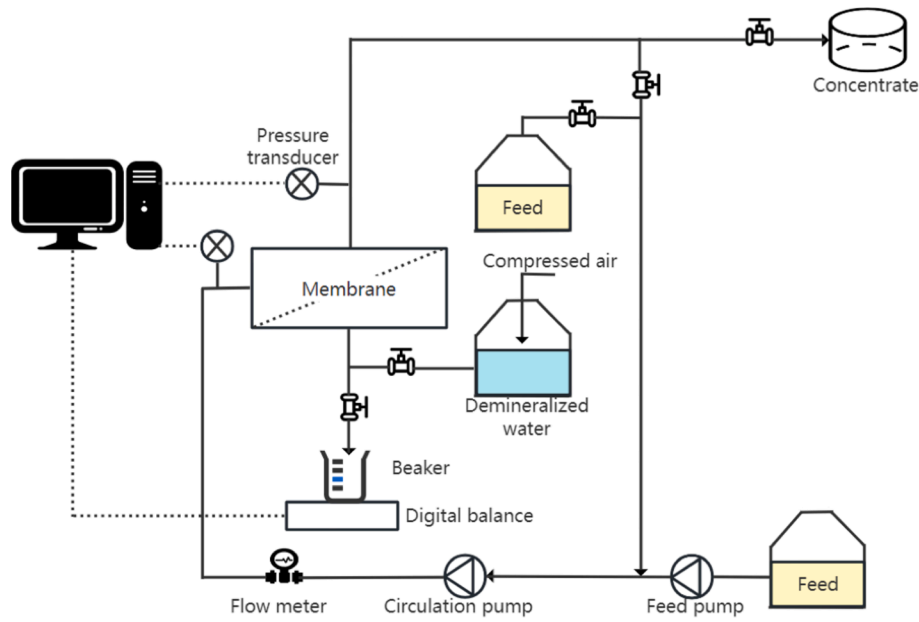
Fig. 1. Schematic view of filtration set up with constant flux.

consisted of six cycles, each with three stages. The first stage was to filtrate the PW at a specific flux for 20 min. In the second stage, the fouled membranes were backwashed at a constant backwash flux, being approximately 1050 Lm^{-2}h^{-1}. Based on the membrane's permeability, the fouled A0 and A20 membranes were backwashed for 30 s with demineralized (DI) water under 3 and 5.25 bar, respectively. The third stage involved forward flushing the membrane with feed PW water for 15 s at a CFV of 0.8 m/s to remove and replace the feedwater.

2.6.2. Data analysis

The fouling resistance of the pristine A0 and coated A20 membranes was calculated based on the resistance-in-series model [34,35], as shown in Eq. (1), Eq (2), Eq. (3), Eq. (4) and Eq. (5):

$$R_t = \frac{TMP}{\mu J} = R_m + R_r + R_{ir} \tag{1}$$

$$R_m = \frac{TMP_0}{\mu J} \tag{2}$$

$$R_t = \frac{TMP_1}{\mu J} \tag{3}$$

$$R_{ir} = \frac{TMP_2}{\mu J} - \frac{TMP_0}{\mu J} \tag{4}$$

$$R_r = R_t - R_m - R_{ir} \tag{5}$$

$$TMP_{Normalized} = \frac{TMP}{TMP_0} \tag{6}$$

Where TMP_0 represents the TMP needed to achieve the required flux with a clean membrane, TMP_1 refers to the TMP after each cycle, and TMP_2 reflects the TMP following the backwash processes, R_t (m^{-1}), R_r, R_{ir}, R_m denotes the overall resistance, reversible fouling resistance, irreversible fouling resistance, and intrinsic membrane resistance. The value of R_m was obtained by conducting filtration experiments using DI water. The value of R_t was calculated by using the final filtration pressure at the end of each filtration cycle. After backwashing the fouled membranes using DI water for 30 s, the R_{ir} was calculated by subtracting the TMP_0 from TMP_2 and then dividing the result by the viscosity and permeate flux. The R_r value was then determined by subtracting the sum

of R_{ir} and R_m from R_t. The normalized TMP was calculated using the TMP to divide the TMP_0, as indicated in Eq. (6).

3. Results and discussion

3.1. Characteristics of the raw produced water

Characteristics of the real PWs are shown in Table 1. The results indicate that PW B contained higher levels of COD (22670 ± 524 mg/L) than PW A (9160 ± 168 mg/L). The conductivity of PW A (51.2 ± 2.6 mS/cm) was comparable to that of the feed water in a seawater desalination plant (52.8 ± 0.2 mS/cm) [36]. By comparison, PW B's conductivity (142.1 ± 4.2 mS/cm) and TDS (105567 ± 1066 mg/L) were about three times higher than those of seawater and similar to those of the PW from a well site in Midland, USA [6]. Based on the particle size distribution analyses of the PW, the mean particle sizes of PW A and B were 0.24 ± 0.09 and 4.85 ± 0.84 μm, respectively (Fig. 2). For PW A, particles smaller than 10 μm accounted for 90.6 % of the total volume; for PW B, this proportion was only 59.4 % (Fig. 2). The difference in water characteristics between the two PWs may lead to varying degrees of membrane fouling.

3.2. Fouling of membranes by synthetic O/W emulsions at various salinities

The effect of the salinity on the fouling of both membranes (A0 and A20, respectively) was conducted by adding 10^{-3} M NaCl, 10^{-2} M NaCl, and 10^{-3} M NaCl + 10^{-3} M CaCl$_2$ to the O/W emulsions stabilized with SDS (Fig. 3). As shown in Fig. S5, these emulsions had similar particle

Table 1
Characteristics of the raw PW.

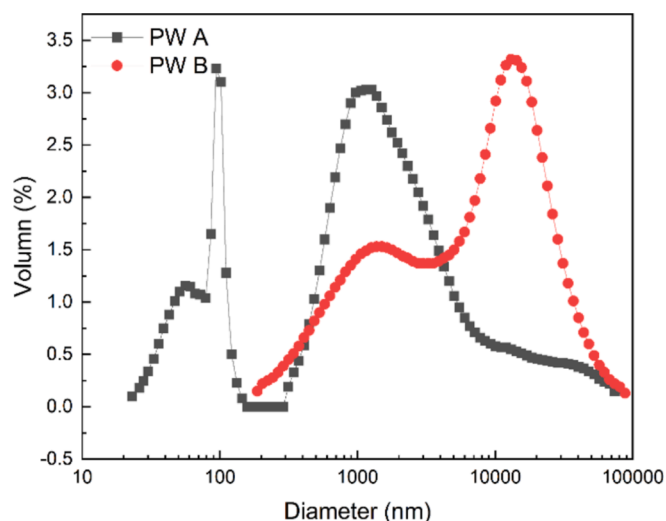| Parameters	Raw (PWA)	Raw (PW B)
Turbidity	234 ± 19	4032 ± 62
pH	7.44 ± 0.29	8.29 ± 0.21
Conductivity (mS/cm)	51.7 ± 2.6	142.1 ± 4.2
COD (mg/L)	9160 ± 168	22670 ± 524
TOC (mg/L)	1856 ± 47	5335 ± 122
Mean particle size (μm)	4.22 ± 0.09	11.31 ± 1.84
TDS (mg/L)	30833 ± 1389	105567 ± 1066
TSS (mg/L)	4567 ± 1327	8067 ± 2185

Fig. 2. The particle size distribution of the (a) PW A and (b) PW B.

size distributions. It can be observed that the fouling in the A20 membrane appeared to be lower, compared to the A0 membrane, probably due to the more negatively charged surface. With the addition of NaCl from 10^{-1} M to 10^{-3} M (Fig. 3 a-b,d,f), the fouling of the A0 and A20 membranes increased as the salinity increased. This increased fouling can be explained by the compression of the diffuse double layer of positive ions around the negative oil droplet and the simultaneous compression of the diffuse double layer on the surface of the negatively charged membrane with increased salinity and thus ionic strength, resulting in a lower negative charge of both the O/W emulsion and the membrane [37]. The above explanation is supported by the results of the

absolute values of the zeta potential of the O/W emulsion, which showed a decrease from -50.7 ± 0.6 mV to -31.5 ± 0.8 mV, respectively, with an increase in salinity from 10^{-1} M to 10^{-3} M (Table.S1). In the meantime, as depicted in Fig. 3e, the zeta potentials of the A0 and A20 membranes decreased from 50.1 ± 1.6 mV to -17.6 ± 1.5 mV and -55.4 ± 1.2 mV to -25.5 ± 1.3 mV, respectively. The A0 membrane surface charge changed from slightly positive (3.0 ± 0.5 mV) to highly negative (-50.1 ± 1.6 mV) probably due to the adsorption of the SDS [26]. The surfactant molecules form a layer at the surface of the hydrophilic A0 membrane, with their negative head groups oriented toward the surface. Subsequently, the second layer is adsorbed on the first layer, orienting the adsorbed surfactant with the negatively charged, hydrophilic head groups to the solvent, making the hydrophilic surface even more hydrophilic and negatively charged [38]. The results are consistent with previous studies, which reported that the absolute zeta potential of the membrane decreased with the increase in salinity [37,39,40]. The WCA increased from $27° \pm 1.2°$ to $54° \pm 2.6°$ (Table. S1) with the salinity increase from 10^{-1} M to 10^{-3} M, indicating sodium ions interacted with the hydrophilic group of the membrane surface, and that the salinity affected the hydrogen-bonding structures of the O/W emulsions [41].

With the addition of the Calcium ions (Ca^{2+}), irreversible fouling was higher than at other salinity levels (Fig. 3c and Fig. 3f). Ca^{2+} are commonly present in PW, while membrane fouling can be accelerated by divalent cations such as Ca^{2+}, which cause the diffuse double layer to compress more than monovalent ions [42]. In addition, Ca^{2+} and the sulfate group of SDS may react with each other, forming a complex [43,44], thus increasing the irreversible fouling [45]. However, the irreversible fouling of the A20 membrane was still lower than that of the A0 membrane (Fig. 3c) since a lower zeta potential of the A20 membrane (-29.4 mV), compared to the A0 membrane (-19.0 mV), was measured (Fig. 3e), although the repulsion was weaker than without

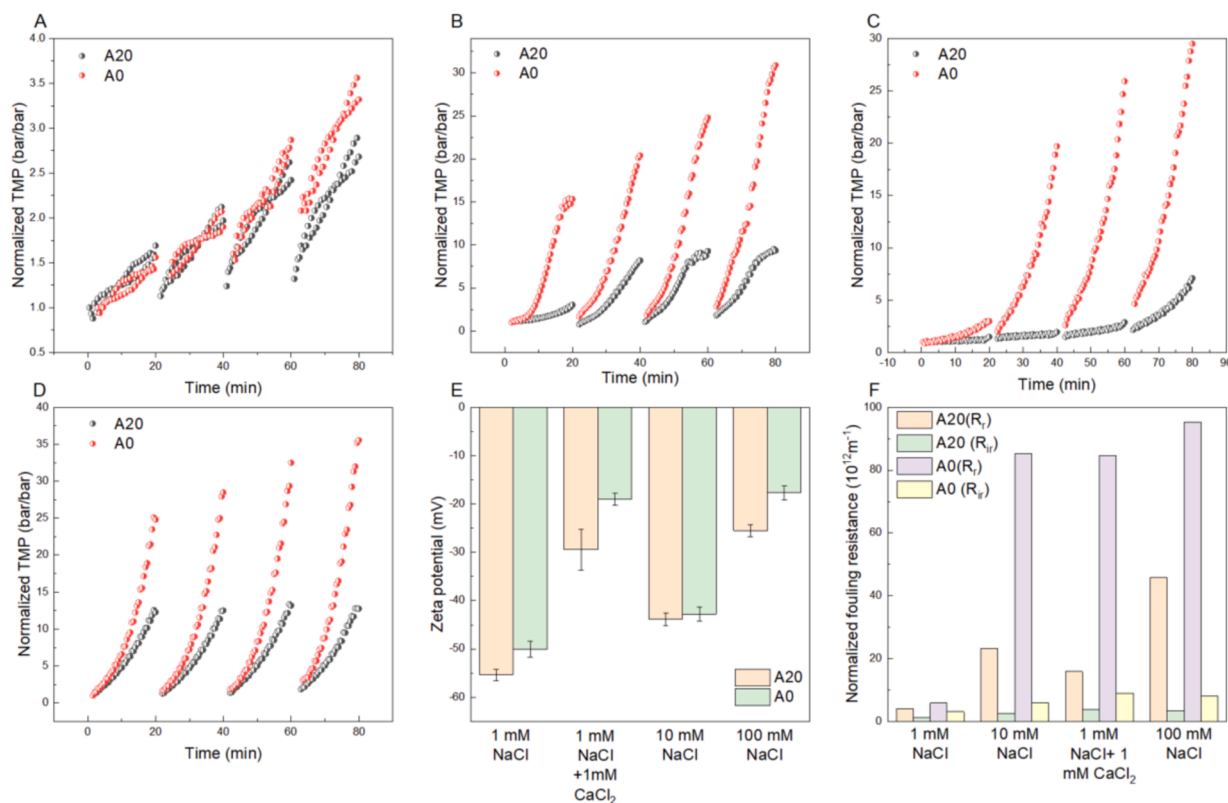**Fig. 3.** The normalized TMP curves of the A0 and the A20 membrane during the filtration of synthetic O/W emulsions at varying salinity: (a) 10^{-3} M NaCl, (b) 10^{-2} M NaCl, (c) 10^{-3} M NaCl + 10^{-3} M CaCl$_2$, (d) 10^{-1} M NaCl. (e) Zeta potential of the A0 and A20 membranes with varying salinity and ion compositions. (f) The normalized resistance of the A0 and A20 membranes.

adding Ca^{2+}.

3.3. Effects of flux on membrane fouling by real produced water

The threshold flux of the A0 and A20 membrane, when filtering PW B, were 39 and 42 $Lm^{-2}h^{-1}$, respectively (Fig. S6), thus, three distinct permeate fluxes were chosen, approximately at and higher than the threshold flux, being 30, 40, and 50 $Lm^{-2}h^{-1}$, respectively, to study the effect of permeate flux on membrane fouling by PW B (Fig. 4). At a flux of 30 $Lm^{-2}h^{-1}$, which was lower than the threshold flux, the interactions between foulants and membrane led to pore blockage of the A0 membrane, followed by the formation and continuous growth of the reversible cake layer on the membrane surface [46]. However, the SiC coating probably inhibited the deposition of the hydrophobic foulants, slowing down the cake layer formation. In addition, the starting point of the normalized water permeance curves of the A0 membrane showed a downward shift with each cycle, this trend was not observed in the A20 membrane, indicating that irreversible fouling existed in the A0 membrane and not in the A20 membrane (Fig. S7 a and b). When the flux exceeded the threshold flux (50 $Lm^{-2}h^{-1}$), the interactions between the foulant and the deposited foulant probably represented the dominant fouling mechanism, which is supported by the FBI-SEM images as presented in Section 3.6, leading to the formation of an (oily) cake layer and a consequent rapid increase in TMP. At the same time, the high TMP probably led to the compaction of the cake layer, and forced the small-sized foulants into the membrane pores, leading to increased irreversible fouling of the A0 and A20 membranes, as confirmed by every cycle's lower initial normalized permeance (Fig. S7 c). At this high flux, hydraulic cleaning is still effective in removing the foulant cake layer, which can be confirmed by the relatively low irreversible fouling compared with reversible fouling and the high permanence recovery (PR). The normalized permeance (64 % PR) of the A20 membrane was still higher than that of the A0 membrane (47 % PR) in the final cycle at 50 $Lm^{-2}h^{-1}$ (Fig. S7). Moreover, the PR of the A20 membrane after backwashing with DI water was as high as 95 ± 2 % of the original permeability at 40 $Lm^{-2}h^{-1}$, suggesting promising backwashing efficiencies and implying its suitability for long-term separation of the PW (Fig. S7). In addition, Fux and Ramon have reported that during filtration experiments at fluxes lower than the threshold flux, the oil droplets are spherical, and can be easily removed by forward crossflow flushing. However, when the flux exceeds the threshold flux, the droplets deform and cause irreversible fouling inside the membrane pores [47].

3.4. Effects of crossflow velocities on membrane fouling

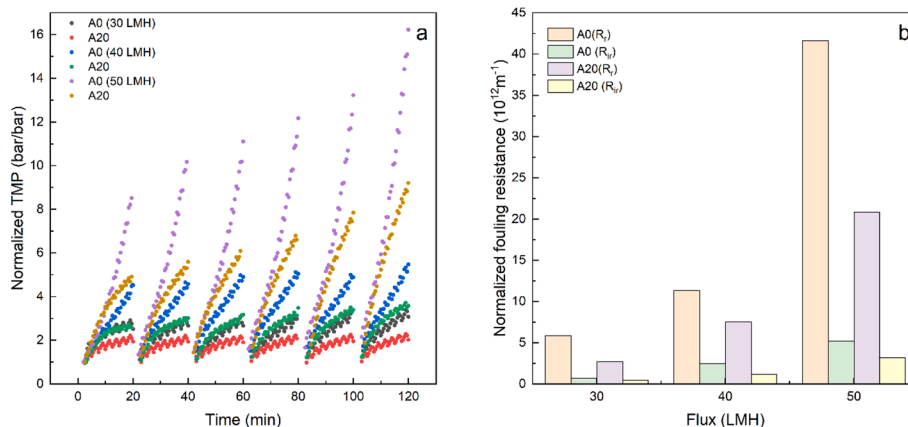The membrane filtration performances, filtering PW B under different CFVs (0.4, 0.8, and 1.2 m/s) were compared at 50 $Lm^{-2}h^{-1}$. This high flux is preferred in full-scale installations because a smaller membrane surface is needed to treat PW. At low CFV (0.8 m/s), the higher TMP at the constant flux of 50 L $m^{-2}h^{-1}$ probably compacted the cake foulants, thereby facilitating the development of a denser, low porosity cake layer [48], impacting permeability, since the hydraulic resistance of the cake layer is highly influenced by its porosity. As shown in Fig. 5a, increasing the filtration CFVs from 0.8 to 1.2 m/s reduced the TMP increase rate (dTMP/dt), thus alleviating membrane fouling, as also reported by Hube et al. [49]. The reversible fouling was dominant for both the A0 and A20 membranes (Fig. 5b). However, much higher reversible fouling was observed for the A0 membrane than for the A20 membrane at different CFVs. The A20 membrane, for example, exhibited much lower reversible fouling (22.1×10^{12} m^{-1}) than the A0 membrane (54.9×10^{12} m^{-1}) at the CFV of 0.8 m/s. This can be explained by the higher hydrophilicity of the A20 membrane compared to the A0 membrane, which is confirmed by the WCA, decreasing from 37° (A0) to 18° (A20) (Fig.S8). Since the zeta potential of the PW is close to 0 mV when the salinity of PW is higher than 50,000 mg/L [19], a low adhesion to the hydrophilic A20 membrane therefore led to a thin cake layer. The reversible fouling further decreased from 16.88×10^{12} m^{-1} to 3.97×10^{12} m^{-1} for the A20 membrane when the CFV increased from 0.8 m/s to 1.2 m/s, respectively (Fig. 5b). The increased turbulence and shear forces close to the membrane surface apparently reduced the concentration polarization, preventing further accumulation and deposition of foulants onto the membrane [50]. This is supported by an increase of the Reynolds number (Re) from 3573 to 5359 (Table.S2), and the flow patterns changed from Laminar-turbulent flow to turbulent flow since the turbulent flow is typically characterized as Re greater than 4000 [51]. In addition, the oil rejection by the A0 membrane increased from 98.4 ± 0.3 % to 99.0 ± 0.5 % with an increase in CFV from 0.4 m/s to 0.8 m/s, indicating an increased oil droplet concentration near the membrane at lower CFV, see Fig. S9b. This phenomenon was also observed for PW A (Fig. S10b), where the oil rejection increased from 96.5 ± 0.6 to 98.2 ± 0.4 % at CFVs of 0.4 m/s and 0.8 m/s, respectively, while high CFVs lead to much higher consumption. It thus indicates a cross-flow (0.8 m/s) of Reynolds number about 3573 as an optimal cross-flow regime.

3.5. Effects of membrane pore size on membrane fouling

At the constant pressure filtration mode, Liu et al. reported that MF membranes with larger pore sizes are more susceptible to membrane fouling compared to UF membranes when filtering the PW [52]. However, in the present study, the UF membrane (A0, A20) showed higher fouling tendencies compared with the MF membrane (A0-600, A20-
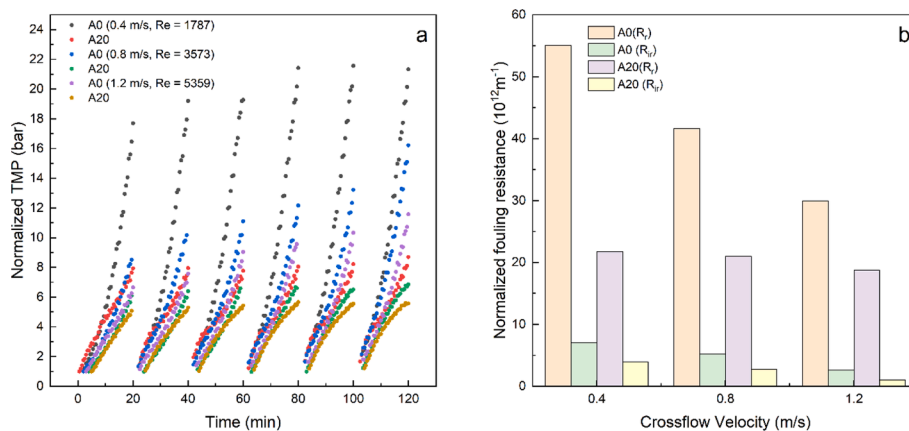

Fig. 4. The normalized (a) fouling curve and (b) resistance of the A0 and A20 membranes for the filtration of PW B at the flux of 30, 40, and 50 L m^{-2}h^{-1} with CFV of 0.8 m/s.

Fig. 5. The normalized (a) fouling curve and (b) resistance of the A0 and A20 membranes for the filtration of PW B at the CFVs of 0.4, 0.8, and 1.2 m/s at 50 L m^{-2}h^{-1}.

600), as shown in Fig. 6a. The observed, initial sharp permeance decline can be explained by adsorption and deposition of foulants smaller than the membrane pore sizes into these pores, followed by a slow and steady permeance decline due to the progressive cake layer formation on the membrane surface [53]. As can be observed, the cake layer only partly covered the A0-600 membrane surface at the end of the filtration cycle (Fig. 7a). In addition, it can be observed that the cake layer surface was rough (Fig. 7b), with a thickness of 1.5 μm, and the sandwich structure of the cross section of the membrane is visible, with the three layers representing the porous cake layer, pore blockage, and open pores (Fig. 7c and d). Finally, it can be observed that oil rejection increased as membrane pore sizes decreased (Fig. S9c), and the A0 (41 nm) and A20 membrane (35 nm) achieved oil removal efficiencies of 99.5 ± 0.3 % and 99.7 ± 0.2 %, respectively (Fig. S9c).

The A20-600 (139 nm) and A0-600 (181 nm) membranes showed the lowest oil rejection percentages, being 98.2 ± 0.2 % and 97.6 ± 0.3 %, respectively (Fig. S9c). This can be explained by the oil droplets forming a cake layer on the membrane surface, which effectively helps reject small-sized oil droplets. The formation of the cake layer was assessed by measuring the oil rejection at the following time intervals: 0 to 3, 3 to 6, and 6 to 20 min in the initial experiment cycle. The results (Fig. S11) indicated a slight increase in oil rejection from 94.3 ± 0.5 % to 98.4 ± 0.3 % for the A0-600 membrane in the initial cycle, which verified the cake layer formation. The significant proportion of external fouling, which accounts for 95.2 % of the total fouling resistance (Fig. 6), confirmed that cake filtration was the dominant fouling mechanism, and

the fouling alleviation was enhanced by increasing pore size. A similar trend was noted in the A20-200, A0-600, and A20-600 membranes. The particle size of the particles in the permeate was close to the average pore size of the membranes, as shown in Table.S3, indicating the size exclusion played a critical role in rejecting particles in the feed. Additionally, there was a reduction in irreversible fouling with increasing pore sizes since, at larger pore sizes, a lower TMP led to less deformation of the oil droplets, so they were not pressed into the pores. Given the fouling resistance and the excellent oil rejection with 99.4 ± 0.3 % (PW B) after cake layer formation, the A20-200 membrane was an optimal choice for separating the PW B. However, for PW A with a smaller size distribution at 11.7 % of the size below 80 nm (Fig. 2), the oil rejection for the A20, A20-200, and A20-600 membranes was 99.1 ± 0.4 %, 96.9 ± 0.5 %, and 89.6 ± 1.5 %, respectively (Fig.S10 and Fig.S12). The A20 membrane is therefore a promising choice. These findings indicated that choosing membranes with appropriate pore sizes should be prioritized over a high initial permanence to achieve low fouling tendency and considerable separation efficiency.

3.6. Characterization of the fouling layer

SEM analysis was performed on the virgin and fouled A0 and A20 membranes to characterize the chemical components and structures of organic components in the cake layers. The top-view surface image of the virgin A0 and A20 membranes shows a porous structure (Fig. 8a and c). In addition, the FIB-SEM images show that, after a filtration time of 3
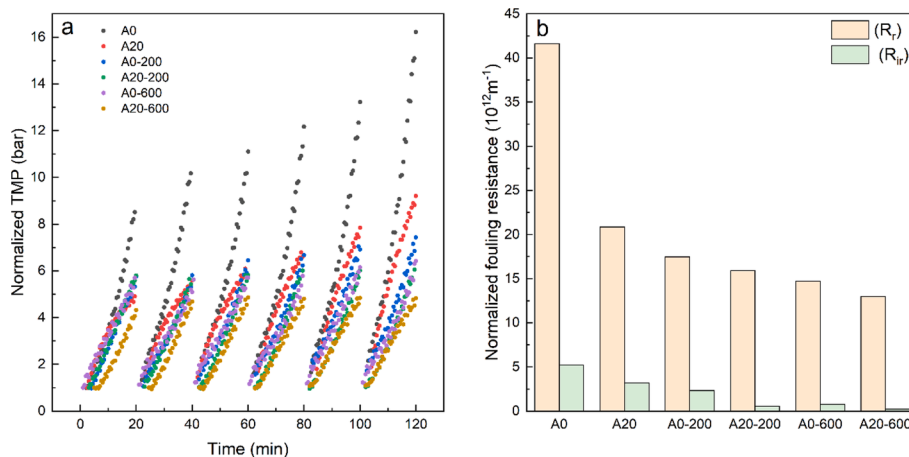

Fig. 6. The normalized (a) fouling curve and (b) resistance of the Al$_2$O$_3$ membranes (A0, A0-200, A0-600) and the SiC-coated membranes (A20, A20-200, A20-600) for the filtration of PW B at 40 L m^{-2}h^{-1} with the CFV of 0.8 m/s.
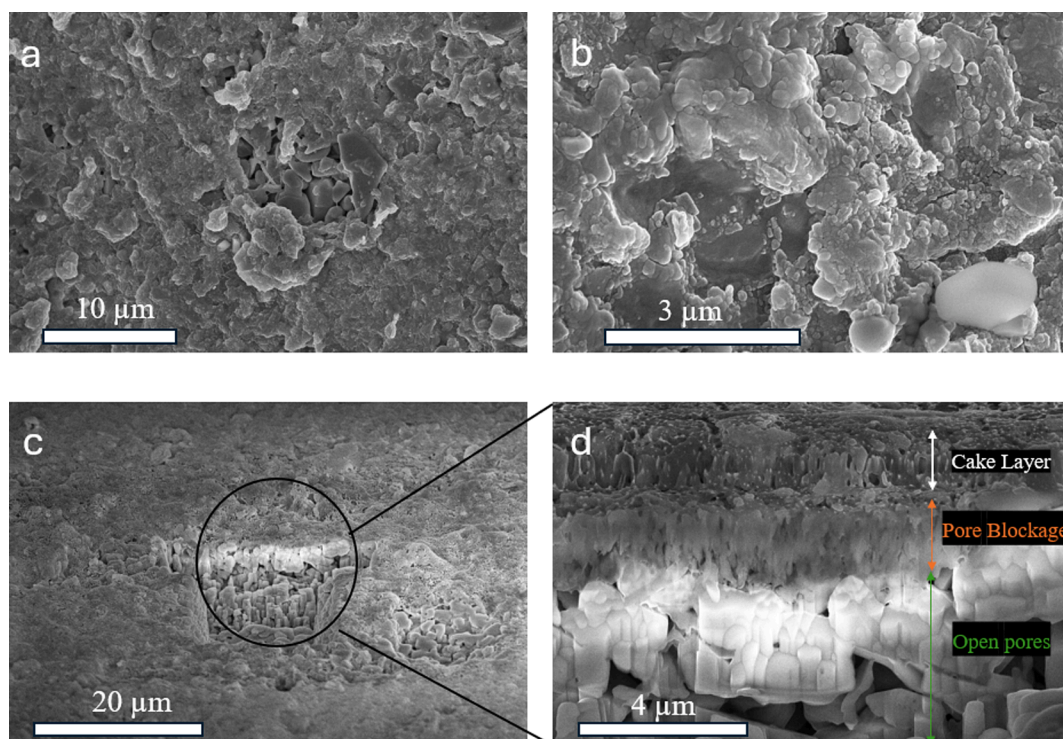
Fig. 7. Top view SEM images of fouled A0-600 membrane with a scale bar of (a) 10 μm and (b) 3 μm. The cross-section FIB-SEM image of A0-600 membrane with a scale bar of (c) 20 μm and (b) 4 μm.

min, a cake layer was not formed on the surface of the A0 membrane, and the thickness of the pore blockage area was only 1 μm (Fig. 8 e-h). However, as depicted in Fig. 8 h, a cake layer with a thickness of 4 ± 1 μm was formed on the A0 membrane with 3–5 μm pore blockage depth after a filtration time of 20 min because the fouling layer was compressed by the permeate drag force and hydraulic pressure [54],

indicating the severe fouling induced by the foulants. This fouling layer was confirmed by the EDAX line scan of element C for the cross section of the A0 membrane (Fig.S13). During the vacuuming stage of the SEM sample preparation, the loss of volatile component resulted in the visualization of a fouling layer being composed of colloidal (e.g. the heavier hydrocarbons existing in crude oil [55]), KCl/NaCl crystals and
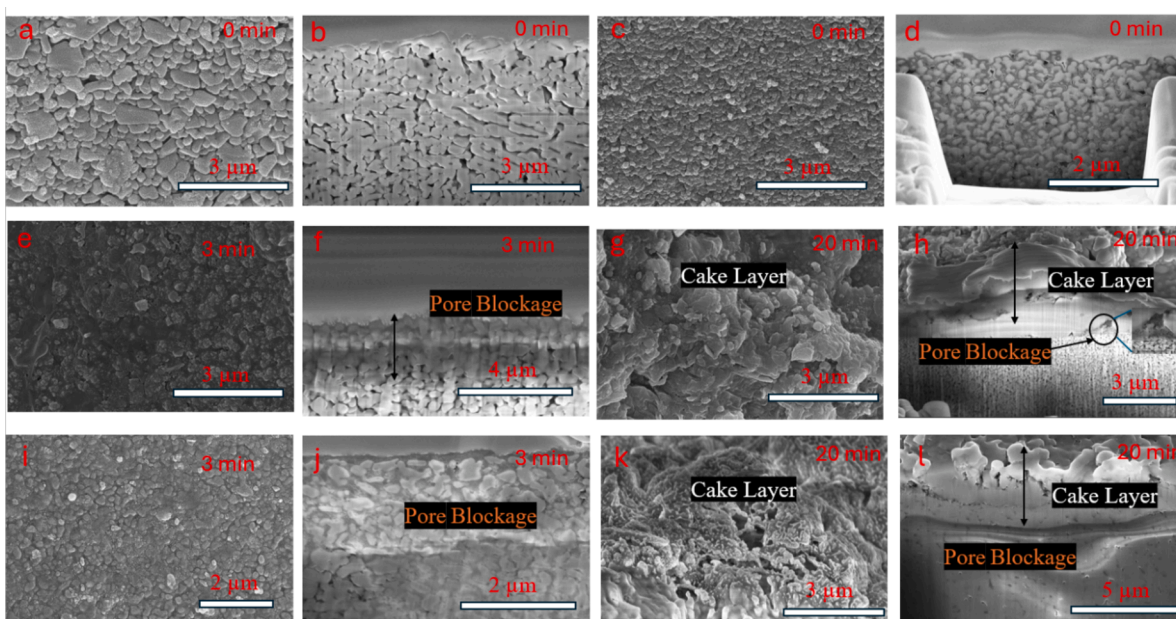

Fig. 8. (a) Top view SEM images and (b) cross-section FIB-SEM images of the clean A0 membrane. (c) Top view SEM images and (d) cross-section FIB-SEM images of the clean A20 membrane. (e) Top view SEM images and (f) cross-section FIB-SEM images of the fouled A0 membrane at the filtration time of 3 min. (g) Top view SEM images and (h) cross-section FIB-SEM images of the fouled A0 membrane at the filtration time of 20 min. (i) Top view SEM images and (j) cross-section FIB-SEM images of the fouled A20 membrane at the filtration time of 3 min. (k) Top view SEM images and (l) cross-section FIB-SEM images of the fouled A20 membrane at the filtration time of 20 min.

non-volatile organic foulants, as indicated by the EDAX analysis of the foulant layer (Fig.S14) and ions in the feed water (Table.S4), since, amongst others, the elements C, O, Fe, Na, Mg, Al, Si, Cl, K, and Ca, were found in the foulant layer. According to the EDAX analysis, organic compounds (23.61 %) were predominant (Fig. S14). Meanwhile, the A20 membrane exhibited moderate fouling, characterized by a loosely attached porous cake layer covering its surface after a filtration time of 20 min (Fig. 8k). These observations confirmed that pristine Al_2O_3 membranes were more susceptible to fouling. The PW is alkaline (pH = 8.4), causing inorganic salts to precipitate and resulting in membrane fouling [56]. The results of the element mapping also showed that K and Cl had a similar distribution, probably due to the formation of the KCl crystals in the dried membrane samples (Fig.S15). The membrane surface of both A0, and A20 membranes after backwash was clean, and fouling was not observed (Fig. S16). The support layer of the A0 membrane also remained clean without observable foulants (Fig. S17), which confirms that the oil droplets probably did not deform and pass through the membrane pores in the condition that TMP is smaller than the critical pressure [57]. As shown in Fig. S18, the microporous structure and the internal fouling of the A0 membrane in the top of the separation layer were not visible in the FE-SEM images, due to limitations in the cutting techniques, which resulted in an uneven membrane cross-section. Further surface polishing was needed for visualization. Overall, the FIB-SEM images offer a clear visualization of the evolution of membrane fouling, allowing for a quantitative assessment, and comparing the fouling of the A0 and A20 membranes.

3.7. Comparison of membrane fouling with two types of oily wastewater

The threshold flux of the A0 and A20 was 41 $Lm^{-2}h^{-1}$ and 48 $Lm^{-2}h^{-1}$, respectively, for the filtration of PW A (Fig.S19), which was higher than when filtering PW B. Fig. 9 shows that with a higher salinity and COD (PW B), compared with PW A, a higher (ir) reversible fouling can be observed for both the A0 and A20 membranes. A dense and compact cake layer was probably formed when filtering PW B due to the electrostatic shielding effect [58]. In addition, the decreased electrostatic repulsion between the foulants and membrane surface reduced the distance between the droplets, and promoting coalescence of the droplets [59]. However, the A20 membrane still exhibited a lower (ir) reversible fouling compared to the A0 membrane.

The oil rejection of PW A (99.3 ± 1.1 %) was a little lower than the oil rejection of PW B (99.6 ± 0.5 %), probably due to the smaller oil droplet sizes, see Fig. 2. The COD oil rejection of the PW A by the A0 and A20 membranes was 78.9 ± 2.7 % and 76.4 ± 1.6 %, respectively, which is also lower than the oil rejection PW B, with 81.7 ± 1.1 % for the A20 membrane and 78.7 ± 1.3 % for the A0 membrane, respectively (Fig.S20 and Fig.S21). The TSS concentration is below 8 mg/L in both the permeate of the A0 and A20 membranes for PW A and PW B, showing a rejection over 99 % (Table S5).

3.8. Long-term filtration performance

Fig. 10 shows that direct ceramic UF of PW using the A20 membranes allowed for a continuous long-term operation of 24 h (72 cycles), under a flux of 40 $Lm^{-2}h^{-1}$ and a CFV of 1.2 m/s. The reversible fouling was dominant and could be easily cleaned by physical cleaning (e.g., backwash). Typically, direct ceramic UF needs regular physical actions such as backwashing combined with chemical cleaning. After immersing the A20 membrane in 0.1 M sodium hydroxide and 0.1 M citric acid for 1 h, respectively, the irreversible fouling was effectively removed, and the permeability of the A20 membrane was recovered to 98.2 ± 0.4 %.

3.9. Comparison of the ceramic MF/UF membrane for PW treatment

Table 2 summarizes various hydrophilic ceramic membranes used for PW treatment, highlighting their pore size, filtration mode, and oil rejection performance. The SiC-deposited membranes fabricated in this study exhibit smaller pore sizes and demonstrate effective oil removal at various salinity and COD levels compared to ceramic UF/MF membranes. Moreover, to the anthors' knowledge, this study is the first to apply SiC membranes in constant flux mode for PW treatment, utilizing the smallest pore size (35 nm) reported among SiC membrane [14,60].

4. Conclusion

Al_2O_3 and SiC-coated membranes with different pore sizes to treat both synthetic and real oilfield produced waters (PWs) were studied in a constant flux mode. The SiC-coated membrane was successfully operated for one day, only by backwashing the membrane every 20 min, confirming the validity of direct ceramic UF of PW with SiC-coated membranes. In addition, the SiC-coated membrane showed high efficacy in removing organic compounds (>80 %) and inorganic particles (>99 %) with a lower (ir)reversible fouling, compared with Al_2O_3 membranes, induced by size exclusion and electrostatic repulsion, and less adsorption. The permeate with over 99 % oil removal was feasible even after 72 manual cycles (24 h) and met the standards for reinjection
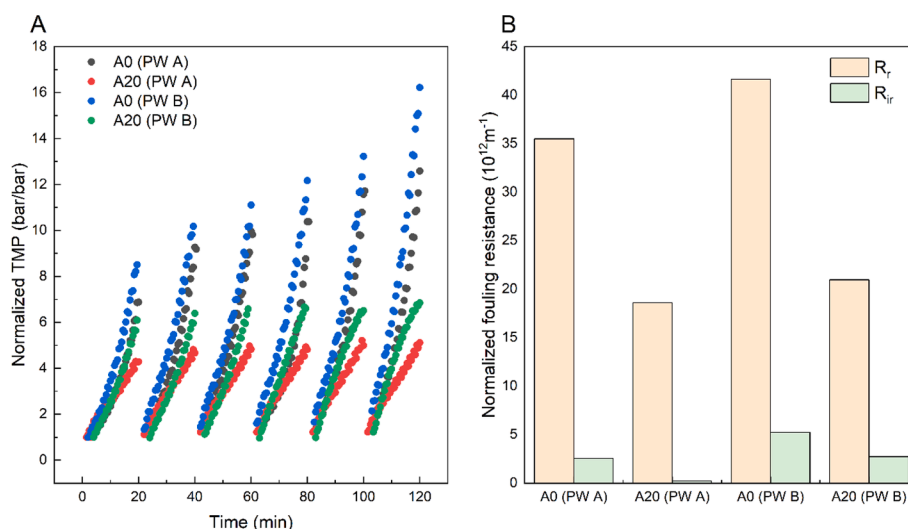

Fig. 9. The normalized (a) fouling curve and (b) resistance of the A0 membranes and the A20 membranes for the filtration of the PW A and the PW B at 50 L m^{-2}h^{-1} with the CFV of 0.8 m/s.

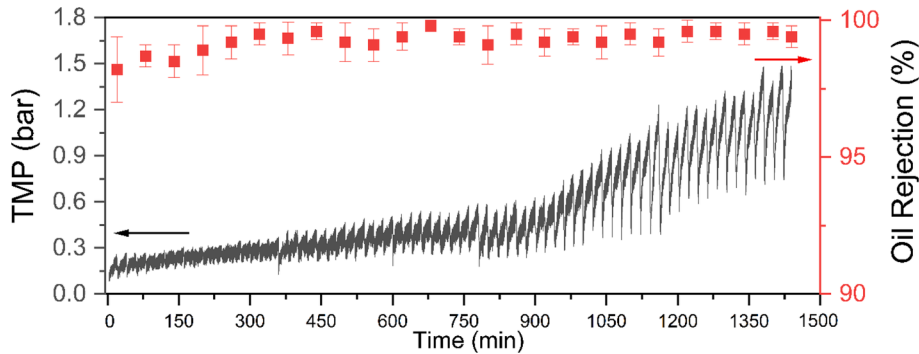**Fig. 10.** The fouling curve of the A20 membranes for 24 h during the filtration of the PW B at the flux of 40 $Lm^{-2}h^{-1}$ with the CFV of 1.2 m/s.

Table 2
Comparison of the ceramic membrane-based PW treatment technologies.

Material	Pore size (nm)	Filtration mode	Oil rejection (%)	Ref
ZrO_2	1000	Constant pressure (2 bar)	>97.22	[61]
ZrO_2-TiO_2	5	Constant pressure (1.4 bar)	>99.9	[62]
ZrO_2	78	Constant pressure (1 bar)	98.8	[11]
Al_2O_3	200	Constant pressure (2.5 bar)	99	[63]
TiO_2	50	Constant pressure (0.4 bar)	80	[14,60]
SiC	500	Constant pressure (0.4 bar)	73	[14,60]
SiC-deposited	139	Constant flux (40 $Lm^{-2}h^{-1}$)	97.6	This work
SiC-deposited	62	Constant flux (40 $Lm^{-2}h^{-1}$)	98.2	This work
SiC-deposited	35	Constant flux (40 $Lm^{-2}h^{-1}$)	99.7	This work

or reuse in future desalination processes. The fouling mechanisms in SiC-coated and Al_2O_3 membranes were also analyzed with the help of FIB-SEM imaging, concluding that pore blockage was the initial fouling mechanism, and (reversible) cake layer fouling dominated the rest of the filtration cycle for both the SiC-coated and the Al_2O_3 membranes. Finally, it was concluded that employing the SiC coating and selecting the appropriate pore size (62 nm A0-200), and CFV (0.8 m/s) based on the properties of the PW is beneficial for fouling mitigation, potentially advancing the utilization of UF in treating PW for reuse purposes.

CRediT authorship contribution statement

Guangze Qin: Conceptualization, Data curation, Investigation, Methodology, Writing – original draft. **Yiman Liu:** Data curation. **Luuk C. Rietveld:** Writing – review & editing, Supervision. **Sebastiaan G.J. Heijman:** Writing – review & editing, Conceptualization, Resources, Supervision.

Declaration of competing interest

The authors declare that they have no known competing financial interests or personal relationships that could have appeared to influence the work reported in this paper.

Appendix A. Supplementary data

Supplementary data to this article can be found online at https://doi.org/10.1016/j.seppur.2025.131841.

Data availability

Data will be made available on request.

References

[1] L. Cheng, A.R. Shaikh, L.F. Fang, S. Jeon, C.J. Liu, L. Zhang, H.C. Wu, D.M. Wang, H. Matsuyama, *Fouling-Resistant and Self-Cleaning Aliphatic Polyketone Membrane for Sustainable Oil-Water Emulsion Separation*, ACS Appl Mater Interfaces 10 (51) (2018) 44880–44889, https://doi.org/10.1021/acsami.8b17192.

[2] Q.Q. Zeng, X.L. Zhou, L.G. Shen, D.L. Zhao, N. Kong, Y.B. Li, X.F. Qiu, C. Chen, J. H. Teng, Y.C. Xu, H.J. Lin, *Exceptional self-cleaning MXene-based membrane for highly efficient oil/ water separation*, J. Membr. Sci. 700 (2024) 122691, https://doi.org/10.1016/j.memsci.2024.122691.

[3] C. Zhao, J. Lei, F. Han, T. Jiao, Y. Han, W. Zhou, *Novel strategy for treating high salinity oilfield produced water: Pyrite-activated peroxymonosulfate coupled with heterotrophic ammonia assimilation*, Water Res 247 (2023) 120772, https://doi.org/10.1016/j.watres.2023.120772.

[4] C. He, X. Wang, W. Liu, E. Barbot, R.D. Vidic, *Microfiltration in recycling of Marcellus Shale flowback water: Solids removal and potential fouling of polymeric microfiltration membranes*, J. Membr. Sci. 462 (2014) 88–95, https://doi.org/10.1016/j.memsci.2014.03.035.

[5] M. Jebur, Y.-H. Chiao, K. Thomas, T. Patra, Y. Cao, K. Lee, N. Gleason, X. Qian, Y. Hu, M. Malmali, S.R. Wickramasinghe, *Combined electrocoagulation-microfiltration-membrane distillation for treatment of hydraulic fracturing produced water*, Desalination 500 (2021) 114886, https://doi.org/10.1016/j.desal.2020.114886.

[6] A. Alborzi, I.M. Hsieh, D. Reible, M. Malmali, *Analysis of fouling mechanism in ultrafiltration of produced water*, J. Water Process Eng. 49 (2022) 102978, https://doi.org/10.1016/j.jwpe.2022.102978.

[7] I.M. Hsieh, A.K. Thakur, M. Malmali, *Comparative analysis of various pretreatments to mitigate fouling and scaling in membrane distillation*, Desalination 509 (2021) 115046, https://doi.org/10.1016/j.desal.2021.115046.

[8] M. Malmali, P. Fyfe, D. Lincicome, K. Sardari, S.R. Wickramasinghe, *Selecting membranes for treating hydraulic fracturing produced waters by membrane distillation*, Sep. Sci. Technol. 52 (2) (2016) 266–275, https://doi.org/10.1080/01496395.2016.1244550.

[9] S. Al-Amshawee, M.Y.B. Yunus, A.A.M. Azoddein, D.G. Hassell, I.H. Dakhil, H. Abu Hasan, *Electrodialysis desalination for water and wastewater: A review*, Chem. Eng. J. 380 (2020) 122231, https://doi.org/10.1016/j.cej.2019.122231.

[10] A. Butkovskyi, H. Bruning, S.A.E. Kools, H.H.M. Rijnaarts, A.P. Van Wezel, *Organic Pollutants in Shale Gas Flowback and Produced Waters: Identification, Potential Ecological Impact, and Implications for Treatment Strategies*, Environ Sci Technol 51 (9) (2017) 4740–4754, https://doi.org/10.1021/acs.est.6b05640.

[11] X. Wang, K. Sun, G. Zhang, F. Yang, S. Lin, Y. Dong, *Robust zirconia ceramic membrane with exceptional performance for purifying nano-emulsion oily wastewater*, Water Res. 208 (2022) 117859, https://doi.org/10.1016/j.watres.2021.117859.

[12] H. Nagasawa, T. Omura, T. Asai, M. Kanezashi, T. Tsuru, *Filtration of surfactant-stabilized oil-in-water emulsions with porous ceramic membranes: Effects of membrane pore size and surface charge on fouling behavior*, J. Membr. Sci. 610 (2020) 118210, https://doi.org/10.1016/j.memsci.2020.118210.

[13] N. Baig, B. Salhi, M. Sajid, I.H. Aljundi, *Recent Progress in Microfiltration/ Ultrafiltration Membranes for Separation of Oil and Water Emulsions*, Chem. Rec. 22 (7) (2022) e202100320, https://doi.org/10.1002/tcr.202100320.

[14] T. Zsirai, A.K. Al-Jaml, H. Qiblawey, M. Al-Marri, A. Ahmed, S. Bach, S. Watson, S. Judd, *Ceramic membrane filtration of produced water: Impact of membrane module*, Sep. Technol. 165 (2016) 214–221, https://doi.org/10.1016/j.seppur.2016.04.001.

[15] J. Wei, P. Nian, Y. Wang, X. Wang, Y. Wang, N. Xu, Y. Wei, *Preparation of superhydrophobic-superoleophilic ZnO nanoflower@SiC composite ceramic membranes for water-in-oil emulsion separation*, Sep. Purif. Technol. 292 (2022) 121002, https://doi.org/10.1016/j.seppur.2022.121002.

[16] Y. Wei, Z. Xie, H. Qi, *Superhydrophobic-superoleophilic SiC membranes with micro-nano hierarchical structures for high-efficient water-in-oil emulsion separation*, J. Membr. Sci. 601 (2020) 117842, https://doi.org/10.1016/j.memsci.2020.117842.

[17] Z. Wu, Z. Ma, T. Zhu, Y. Wang, N. Ma, W. Ji, P. Nian, N. Xu, S. Zhang, Y. Wei, *Engineering of ceramic membranes with superhydrophobic pores for different size water droplets removal from water-in-oil emulsions*, Sep. Purif. Technol. 353 (2025) 128293, https://doi.org/10.1016/j.seppur.2024.128293.

[18] Z. Pan, S. Cao, J. Li, Z. Du, F. Cheng, *Anti-fouling TiO2 nanowires membrane for oil/ water separation: Synergetic effects of wettability and pore size*, J. Membr. Sci. 572 (2019) 596–606, https://doi.org/10.1016/j.memsci.2018.11.056.

[19] S.E. Weschenfelder, M.J.C. Fonseca, B.R.S. Costa, C.P. Borges, *Influence of the use of surfactants in the treatment of produced water by ceramic membranes*, J. Water Process Eng. 32 (2019) 100955, https://doi.org/10.1016/j.jwpe.2019.100955.

[20] M. Chen, R. Shang, P.M. Sberna, M.W.J. Luiten-Olieman, L.C. Rietveld, S.G. J. Heijman, *Highly permeable silicon carbide-alumina ultrafiltration membranes for oil-in-water filtration produced with low-pressure chemical vapor deposition*, Sep. Purif. Technol. 253 (2020) 117496, https://doi.org/10.1016/j.seppur.2020.117496.

[21] R. Shang, A. Goulas, C.Y. Tang, X. de Frias Serra, L.C. Rietveld, S.G.J. Heijman, *Atmospheric pressure atomic layer deposition for tight ceramic nanofiltration membranes: Synthesis and application in water purification*, J. Membr. Sci. 528 (2017) 163–170, https://doi.org/10.1016/j.memsci.2017.01.023.

[22] Y.M. Lin, C. Song, G.C. Rutledge, *Direct Three-Dimensional Visualization of Membrane Fouling by Confocal Laser Scanning Microscopy*, ACS Appl Mater Interfaces 11 (18) (2019) 17001–17008, https://doi.org/10.1021/acsami.9b01770.

[23] A. Behzad, K. Hooghan, C. Aubry, M. Khan, J. Croue, *SEM-FIB Characterization of Reverse Osmosis Membrane Fouling*, Microsc. Microanal. 17 (S2) (2011) 1768–1769, https://doi.org/10.1017/S1431927611009718.

[24] T. Rodenas, G. Prieto, *FIB-SEM tomography in catalysis and electrochemistry*, Catal. Today 405–406 (2022) 2–13, https://doi.org/10.1016/j.cattod.2022.09.013.

[25] H. Chang, T. Li, B. Liu, R.D. Vidic, M. Elimelech, J.C. Crittenden, *Potential and implemented membrane-based technologies for the treatment and reuse of flowback and produced water from shale gas and oil plays: A review*, Desalination 455 (2019) 34–57, https://doi.org/10.1016/j.desal.2019.01.001.

[26] G. Qin, A. Jan, Q. An, H. Zhou, L.C. Rietveld, S.G.J. Heijman, *Chemical vapor deposition of silicon carbide on alumina ultrafiltration membranes for filtration of microemulsions*, Desalination 582 (2024) 117655, https://doi.org/10.1016/j.desal.2024.117655.

[27] B. Morana, G. Pandraud, J.F. Creemer, P.M. Sarro, *Characterization of LPCVD amorphous silicon carbide (a-SiC) as material for electron transparent windows*, Mater. Chem. Phys. 139 (2–3) (2013) 654–662, https://doi.org/10.1016/j.matchemphys.2013.02.013.

[28] A. Jan, M. Chen, M. Nijboer, M.W.J. Luiten-Olieman, L.C. Rietveld, S.G.J. Heijman, *Effect of Long-Term Sodium Hypochlorite Cleaning on Silicon Carbide Ultrafiltration Membranes Prepared via Low-Pressure Chemical Vapor Deposition*, Membranes 14 (1) (2024), https://doi.org/10.3390/membranes14010022.

[29] Z. He, S. Kasemset, A.Y. Kirschner, Y.H. Cheng, D.R. Paul, B.D. Freeman, *The effects of salt concentration and foulant surface charge on hydrocarbon fouling of a poly (vinylidene fluoride) microfiltration membrane*, Water Res 117 (2017) 230–241, https://doi.org/10.1016/j.watres.2017.03.051.

[30] J. Minier-Matar, E. AlShamari, M. Raja, F. Khan, M. Al-Maas, A. Hussain, S. Adham, *Detailed organic characterization of process water to evaluate reverse osmosis membrane fouling in industrial wastewater treatment*, Desalination 572 (2024) 117128, https://doi.org/10.1016/j.desal.2023.117128.

[31] Eaton, A.D., M.A.H. Franson, A. American Public Health, A. American Water Works, and F. Water Environment, *Standard Methods for the Examination of Water and Wastewater*. 2005: American Public Health Association. Available from: https://books.google.nl/books?id=buTn1rmfSI4C.

[32] P. Le Clech, B. Jefferson, I.S. Chang, S.J. Judd, *Critical flux determination by the flux-step method in a submerged membrane bioreactor*, J. Membr. Sci. 227 (1–2) (2003) 81–93, https://doi.org/10.1016/j.memsci.2003.07.021.

[33] S.P. Beier, G. Jonsson, *Critical flux determination by flux-stepping*, AIChE J 56 (7) (2009) 1739–1747, https://doi.org/10.1002/aic.12099.

[34] B.C. Huang, Y.F. Guan, W. Chen, H.Q. Yu, *Membrane fouling characteristics and mitigation in a coagulation-assisted microfiltration process for municipal wastewater pretreatment*, Water Res 123 (2017) 216–223, https://doi.org/10.1016/j.watres.2017.06.080.

[35] J. Xing, H. Liang, C.J. Chuah, Y. Bao, X. Luo, T. Wang, J. Wang, G. Li, S.A. Snyder, *Insight into Fe(II)/UV/chlorine pretreatment for reducing ultrafiltration (UF) membrane fouling: Effects of different natural organic fractions and comparison with coagulation*, Water Res 167 (2019) 115112, https://doi.org/10.1016/j.watres.2019.115112.

[36] Y.-G. Lee, S. Kim, J. Shin, J. Rho, Y.M. Kim, K.H. Cho, H. Eom, S.-E. Oh, J. Cho, K. Chon, *Sequential effects of cleaning protocols on desorption of reverse osmosis membrane foulants: Autopsy results from a full-scale desalination plant*, Desalination 500 (2021) 114830, https://doi.org/10.1016/j.desal.2020.114830.

[37] S.A. Onaizi, *Effect of salinity on the characteristics, pH-triggered demulsification and rheology of crude oil/water nanoemulsions*, Sep. Purif. Technol. 281 (2022) 119956, https://doi.org/10.1016/j.seppur.2021.119956.

[38] L.A.T. Nguyen, M. Schwarze, R. Schomäcker, *Adsorption of non-ionic surfactant from aqueous solution onto various ultrafiltration membranes*, J. Membr. Sci. 493 (2015) 120–133, https://doi.org/10.1016/j.memsci.2015.06.026.

[39] H.J. Tanudjaja, V.V. Tarabara, A.G. Fane, J.W. Chew, *Effect of cross-flow velocity, oil concentration and salinity on the critical flux of an oil-in-water emulsion in microfiltration*, J. Membr. Sci. 530 (2017) 11–19, https://doi.org/10.1016/j.memsci.2017.02.011.

[40] D. Elzo, I. Huisman, E. Middelink, V. Gekas, *Charge effects on inorganic membrane performance in a cross-flow microfiltration process*, Colloids Surf A Physicochem Eng Asp 138 (2) (1998) 145–159, https://doi.org/10.1016/S0927-7757(96)03957-X.

[41] C. Zhang, Y. Qu, J. Liu, Q. Chen, M. Shao, W. Li, Q. Xu, *Unraveling the role of NaCl on microfiltration fouling: Insights from In situ analysis of dynamic interfacial behaviors*, J. Membr. Sci. 690 (2024) 122223, https://doi.org/10.1016/j.memsci.2023.122223.

[42] J.M. Dickhout, J. Moreno, P.M. Biesheuvel, L. Boels, R.G.H. Lammertink, W.M. de Vos, *Produced water treatment by membranes: A review from a colloidal perspective*, J. Colloid Interface Sci. 487 (2017) 523–534, https://doi.org/10.1016/j.jcis.2016.10.013.

[43] S. Panpanit, C. Visvanathan, S. Muttamara, *Separation of oil–water emulsion from car washes*, Water Sci. Technol. 41 (10–11) (2000) 109–116, https://doi.org/10.2166/wst.2000.0620.

[44] M. Sammalkorpi, M. Karttunen, M. Haataja, *Ionic Surfactant Aggregates in Saline Solutions: Sodium Dodecyl Sulfate (SDS) in the Presence of Excess Sodium Chloride (NaCl) or Calcium Chloride (CaCl2)*, J. Phys. Chem. B 113 (17) (2009) 5863–5870, https://doi.org/10.1021/jp901228v.

[45] E. Virga, B. Bos, P.M. Biesheuvel, A. Nijmeijer, W.M. de Vos, *Surfactant-dependent critical interfacial tension in silicon carbide membranes for produced water treatment*, J. Colloid Interface Sci. 571 (2020) 222–231, https://doi.org/10.1016/j.jcis.2020.03.032.

[46] C.A. Hejase, V.V. Tarabara, *Nanofiltration of saline oil-water emulsions: Combined and individual effects of salt concentration polarization and fouling by oil*, J. Membr. Sci. 617 (2021) 118607, https://doi.org/10.1016/j.memsci.2020.118607.

[47] G. Fux, G.Z. Ramon, *Microscale Dynamics of Oil Droplets at a Membrane Surface: Deformation, Reversibility, and Implications for Fouling*, Environ Sci Technol 51 (23) (2017) 13842–13849, https://doi.org/10.1021/acs.est.7b03391.

[48] D. Jermann, W. Pronk, R. Kagi, M. Halbeisen, M. Boller, *Influence of interactions between NOM and particles on UF fouling mechanisms*, Water Res 42 (14) (2008) 3870–3878, https://doi.org/10.1016/j.watres.2008.05.013.

[49] S. Hube, J. Wang, L.N. Sim, T.H. Chong, B. Wu, *Direct membrane filtration of municipal wastewater: Linking periodical physical cleaning with fouling mechanisms*, Sep. Purif. Technol. 259 (2021) 118125, https://doi.org/10.1016/j.seppur.2020.118125.

[50] H. Wu, C. Sun, Y. Huang, X. Zheng, M. Zhao, S. Gray, Y. Dong, *Treatment of oily wastewaters by highly porous whisker-constructed ceramic membranes: Separation performance and fouling models*, Water Res 211 (2022) 118042, https://doi.org/10.1016/j.watres.2022.118042.

[51] F.L. Hua, Y.F. Tsang, Y.J. Wang, S.Y. Chan, H. Chua, S.N. Sin, *Performance study of ceramic microfiltration membrane for oily wastewater treatment*, Chem. Eng. J. 128 (2–3) (2007) 169–175, https://doi.org/10.1016/j.cej.2006.10.017.

[52] N. Liu, J. Yang, X. Hu, H. Zhao, H. Chang, Y. Liang, L. Pang, Y. Meng, H. Liang, *Fouling and chemically enhanced backwashing performance of low-pressure membranes during the treatment of shale gas produced water*, Sci Total Environ 840 (2022) 156664, https://doi.org/10.1016/j.scitotenv.2022.156664.

[53] W. Tomczak, M. Gryta, *Application of ultrafiltration ceramic membrane for separation of oily wastewater generated by maritime transportation*, Sep. Purif. Technol. 261 (2021) 118259, https://doi.org/10.1016/j.seppur.2020.118259.

[54] L. Zheng, H. Zhong, Y. Wang, N. Duan, M. Ulbricht, Q. Wu, B. Van der Bruggen, Y. Wei, *Mixed scaling patterns and mechanisms of high-pressure nanofiltration in hypersaline wastewater desalination*, Water Res 250 (2024) 121023, https://doi.org/10.1016/j.watres.2023.121023.

[55] G. Chen, J. Lin, W. Hu, C. Cheng, X. Gu, W. Du, J. Zhang, C. Qu, *Characteristics of a crude oil composition and its in situ waxing inhibition behavior*, Fuel 218 (2018) 213–217, https://doi.org/10.1016/j.fuel.2017.12.116.

[56] T. Ahmad, C. Guria, A. Mandal, *A review of oily wastewater treatment using ultrafiltration membrane: A parametric study to enhance the membrane performance*, J. Water Process Eng. 36 (2020) 101289, https://doi.org/10.1016/j.jwpe.2020.101289.

[57] M. Chen, S.G.J. Heijman, L.C. Rietveld, *Ceramic membrane filtration for oily wastewater treatment: Basics, membrane fouling and fouling control*, Desalination 583 (2024) 117727, https://doi.org/10.1016/j.desal.2024.117727.

[58] K. Feng, W. Ma, F. Zhou, C. Si, P. Zheng, P. Sun, Q. Zhang, M. Zhan, W. Jiang, *Antifouling amidoximated polyacrylonitrile-regenerated cellulose acetate composite nanofibrous membranes for oil/water separation: Membrane fabrication, performance and fouling mechanism*, Desalination 577 (2024) 117411, https://doi.org/10.1016/j.desal.2024.117411.

[59] E. Virga, R.W. Field, P.M. Biesheuvel, W.M. De Vos, *Theory of oil fouling for microfiltration and ultrafiltration membranes in produced water treatment*, J. Colloid Interface Sci. 621 (2022) 431–439, https://doi.org/10.1016/j.jcis.2022.04.039.

[60] T. Zsirai, H. Qiblawey, P. Buzatu, M. Al-Marri, S.J. Judd, *Cleaning of ceramic membranes for produced water filtration*, J. Pet. Sci. Eng. 166 (2018) 283–289, https://doi.org/10.1016/j.petrol.2018.03.036.

[61] S.E. Weschenfelder, A.C.C. Mello, C.P. Borges, J.C. Campos, *Oilfield produced water treatment by ceramic membranes: Preliminary process cost estimation*, Desalination 360 (2015) 81–86, https://doi.org/10.1016/j.desal.2015.01.015.

[62] B. Santos, J.G. Crespo, M.A. Santos, S. Velizarov, *Oil refinery hazardous effluents minimization by membrane filtration: An on-site pilot plant study*, J Environ Manage 181 (2016) 762–769, https://doi.org/10.1016/j.jenvman.2016.07.027.

[63] A. Reyhani, H. Mashhadi Meighani, *Optimal operating conditions of micro-and ultra-filtration systems for produced-water purification: Taguchi method and economic investigation*, Desalin. Water Treat. 57 (42) (2016) 19642–19654, https://doi.org/10.1080/19443994.2015.1101714.